Title

A nanoporous capacitive electrochemical ratchet for continuous ion separations

Journal

Nature Materials, 25(6)

ISSN

1476-1122

Authors

Kautz, Rylan

Herman, Alon

Heffernan, Ethan J

et al.

Publication Date

2026-06-01

DOI

10.1038/s41563-026-02511-y

A nanoporous capacitive electrochemical ratchet for continuous ion separations

Rylan Kautz[1†], Alon Herman[2†], Ethan J. Heffernan[1], Keren Shushan Alshochat[2], Eden Grossman[2], Rahul Saxena[2], Camila Muñetón[3,4], David Larson[5,6], Joel W. Ager III[5,6,7,8], Francesca M. Toma[5,6,9,10], Shane Ardo[1,3,11]* and Gideon Segev[2]**

[1]Department of Materials Science & Engineering, University of California Irvine, Irvine, CA 92697, USA
[2]School of Electrical Engineering, Tel Aviv University, Tel Aviv 6997801, Israel
[3]Department of Chemistry, University of California Irvine, Irvine, CA 92697, USA
[4]Department of Chemistry, University of Massachusetts Boston, Boston, MA 02125 USA
[5]Chemical Sciences Division, Lawrence Berkeley National Lab, Berkeley, CA 94720, USA
[6]Joint Center for Artificial Photosynthesis, Lawrence Berkeley National Lab, Berkeley, CA 94720, USA
[7]Materials Sciences Division, Lawrence Berkeley National Lab, Berkeley, CA 94720, USA
[8]Department of Materials Science and Engineering, University of California Berkeley, Berkeley, CA 94720, USA
[9]Institute of Functional Materials for Sustainability, Helmholtz Zentrum Hereon, Teltow, 14513, Germany
[10]Faculty of Mechanical and Civil Engineering, Helmut Schmidt University, Hamburg 22043, Germany
[11]Department of Chemical & Biomolecular Engineering, University of California Irvine, Irvine, CA 92697, USA

*Email: ardo@uci.edu
**Email: gideons1@tauex.tau.ac.il
† These authors contributed equally to this work

Abstract

Directed ion transport in liquid electrolyte solutions underlies many phenomena in natural and industrial settings. While nature has evolved structures that drive continuous ion flow without Faradaic redox reactions, establishing this process in synthetic systems has been challenging. Here we report an ion pump that drives aqueous ions against a force using a capacitive ratchet mechanism independent of redox reactions. Modulation of an electric potential between thin metallic layers on either face of a nanoporous alumina wafer immersed in solution results in persistent voltages and ionic currents. This occurs due to the non-linear capacitive nature of electric double layers, whose repeated charging and discharging sustains a continuous ion flux. Using this approach, we demonstrate ratchet driven electrodialysis that reaches a 50% decrease in the conductivity of the solution in a dilution cell. These ratchet-based ion pumps can enable continuous desalination and selective ion separation using an electrically powered device with no moving parts.

Main

Ratchets are non-equilibrium devices that utilize temporally modulated input signals and spatial asymmetries to drive a steady state particle flux.[1–3] Ratchets have been studied theoretically and experimentally[1,4–8] for electronic signal rectification,[1,4,7,8] to drive net transport of uncharged species through induced-charge electrokinetics,[9] for microparticle and nanoparticle sorting,[10–16] and to drive net ionic current or water pumping by alternating redox reactions.[17–19] A recent theoretical study has shown that ratchet based ion pumps (RBIPs) can sort ions with unprecedented selectivity and desalinate water.[20,21]

An electric double layer forms at the interface between an electrode and a liquid electrolyte and consists of a compact layer of adsorbed solvent molecules and ions, and a diffuse layer of mobile ions. This results in a capacitance that varies with the magnitude of the electrode potential and in response to temporal changes in it.[22–24] These variations in capacitance affect the double layer charging and discharging time constants. Here we utilize this phenomenon to pump ions across a membrane. RBIP membranes are made of nanoporous anodized aluminum oxide (AAO) wafers with thin metal layers, serving as electrodes covering the two wafer surfaces without blocking the pores, thus forming nanoporous capacitor-like structures (Figure 1a-e, Supplementary Figure 1). Details on the RBIP fabrication process can be found in the methods section.

Ion Pumping Mechanism

We start by analyzing the performance of RBIPs in which both surfaces are coated with gold thin films. This configuration is termed Au-Au. Due to the rough and poly-crystalline nature of the gold films covering the AAO wafer (Figure 1b,c), the RBIP surface is inhomogeneous. Moreover, the energetics of Cl^- adsorption processes are facet dependent.[25] Combined with the inherently non-linear nature of double layers,[22] these result in potential-dependent adsorption and charging phenomena on the RBIP surfaces leading to a dispersion of time constants and thus a non-linear capacitance.[23–26] Since no two poly-crystalline surfaces are identical, small differences in the RBIP surface properties result in an unintentional asymmetry, which is essential for ratchet-driven transport.

When an input signal, V_{in}, is applied between the two metal layers, the double layer at one surface is charged while the other is discharged with time constants that are determined by the properties of the input signal, the metal surface, and the aqueous electrolyte. The electrostatic potential difference between the bulk solution and the adjacent metal surface at each side of the RBIP (V_L and V_R in Figure 1a) fluctuates according to these time constants, and the electric potential difference between the bulk of the two electrolyte compartments is:

$$V_{out}(t) = V_L(t) + V_{in}(t) - V_R(t). \quad (1)$$

The RBIP performance was evaluated by placing an RBIP between two compartments of aqueous chloride-containing electrolyte and measuring the voltage between two Ag/AgCl wires, which are immersed in the solution on each side of the RBIP (V_{out}). Because of the extremely high reaction rate for reversible oxidation of Cl^- at Ag to form insoluble AgCl, the voltage difference between the two Ag/AgCl wires is dominated by the electrochemical potential difference of Cl^- at the wire surfaces. The measured resting voltage between the two Ag/AgCl wires, V_{rest}, when both compartments are filled with the same electrolyte (1 – 10 mM Cl^- containing solution) is lower than 10 mV in magnitude and is typically about 3 mV. Application of a DC bias across the RBIP contacts (V_{in} of +300 mV or –300 mV) resulted in the expected

prompt observation of $V_{out} \approx V_{in}$ that decayed to $V_{out} \approx V_{rest}$ over ~1 sec due to capacitive charging. Hence, under these conditions there is no steady state net driving force for ion transport through the RBIP.

To demonstrate the difference in charging and discharging time constants and their contribution to the ratchet output, the voltage signals $V_L(t)$ and $V_R(t)$ were measured while the RBIP was operating. The input signal was a rectangular wave in the form:

$$V_{in}(t) = \begin{matrix} V_a & 0 < t \leq d_c T \\ -V_a & d_c T < t \leq T \end{matrix}, \quad (2)$$

where T is the temporal period and d_c ($\in [0,1]$) is the duty cycle. The charging and discharging time constants of every surface at every part of the period were found by fitting the averaged measured signals to a single exponential charging/discharging function:

$$V(t) = \begin{matrix} V_{f,1} + \left(V_{i,1} - V_{f,1}\right)\exp\left(-\frac{t}{\tau_1}\right) & 0 < t \leq d_c T \\ V_{f,2} + \left(V_{i,2} - V_{f,2}\right)\exp\left(-\frac{t - d_c T}{\tau_2}\right) & d_c T < t \leq T \end{matrix}, \quad (3)$$

where V_i is the initial voltage, and τ is the charging/discharging time constant. V_f is the voltage at which the signal would saturate if the capacitances were linear. A subscript 1 notes the first part of the temporal period ($0 < t \leq d_c T$) and a subscript 2 the second part of the period ($d_c T < t \leq T$).

Because the RBIP is electrically floating (i.e., no part of the system is grounded), charging of one contact is accompanied by discharging of the other (Figure 2a-bFigure 1). Thus, the time constants for charging the right and left surfaces are $\tau_{R,1}$ and $\tau_{L,2}$ respectively, and the time constants for discharging the right and left surfaces are $\tau_{R,2}$ and $\tau_{L,1}$ respectively. Figure 2c shows the extracted time constants for charging and discharging the surfaces as a function of the duty cycle. The other fitted parameters are shown in Supplementary Figure 2. In linear systems the time constants are invariant. However, due to the non-linearity of the double layer capacitances, all time constants vary with the duty cycle. Particularly, there is a significant difference between the charging (and discharging) time constants of the two surfaces: $\tau_{L,1} \neq \tau_{R,2}$ and $\tau_{L,2} \neq \tau_{R,1}$. At a duty cycle of 0.5 the time constants are: $\tau_{L,1} = 6.59$ ms, $\tau_{R,2} = 8.21$ ms, and $\tau_{L,2} = 8.5$ ms, $\tau_{R,1} = 7.23$ ms. This asymmetry implies that a voltage rise due to the charging of a surface at the first part of the period is not fully negated by the charging of the opposite surface during the second part of the period. As a result, a non-zero time-averaged output voltage can be obtained even for time-symmetric input signals. For duty cycles above 0.4 the time constants for charging one surface and discharging the other are similar yet vary significantly between the first part and the second part of the period: $\tau_{L,1} \approx \tau_{R,1} \neq \tau_{L,2} \approx \tau_{R,2}$. A similar analysis for signals with different frequencies and $d_c = 0.5$ shows that the time constants decrease significantly with the signal frequency (Supplementary Note 3). Thus, the charging and discharging dynamics are mostly determined by the duration for charging and discharging. As a result, the difference in charging and discharging time constants is smallest for $d_c = 0.5$, and for this duty cycle the asymmetry is determined only by the non-linear nature of the capacitance with the potential and the difference in the microstructure of the two surfaces.

The net ratchet induced voltage, $\Delta\bar{V}_{out}$, was obtained by finding the mean value of V_{out} while the ratchet is ON and reducing from it the mean value of V_{out} while the ratchet was OFF (see the methods section and Supplementary Note 2 for more details). Figure 2d shows $\Delta\bar{V}_{out}$ as a function of the input signal duty

cycle. Demonstrating the signature output of a flashing ratchet,[1,4] the RBIP output is very low when a constant bias is applied (duty cycle of 0 or 1). However, once the input signal alternates, a net voltage builds up between the two compartments providing a driving force for ion transport. Moreover, $\Delta\bar{V}_{out}$ reaches 29.1 mV for a moderate duty cycle of 0.375 where the time averaged input is -75 mV, and 23 mV for a duty cycle of 0.5 where the time averaged input voltage is 0 V. Since $\Delta\bar{V}_{out}$ is maximal when the time-averaged input voltage is near 0 V, and it is negligible for extreme duty cycles when the magnitude of the time-averaged input voltage is maximal, it can be concluded that the contribution of mechanisms such as conduction, ion electrophoresis and electro-osmosis to $\Delta\bar{V}_{out}$ is minimal. This was further verified by showing that mass transport of water through the membrane is negligible (Figures S18-S19). Furthermore, the amplitude of the input signal is significantly lower than the Gibbs free energy required for water splitting. Hence there are no electrochemical reactions taking place on the electrode surfaces. At such low voltages, even if the voltage is held constant, the applied potential bias supports only the formation of double layers, there is no direct current between the electrodes, the electric field outside the double layers is zero, and there is no electrophoretic ion transport.

Device Performance

Next, we measured the ratchet performance for input signals with various frequencies and duty cycles. The charging and discharging time constants of $V_{out}(t)$ vary significantly with the input signal frequency and duty cycle (Supplementary Note 4). Figure 3a shows $\Delta\bar{V}_{out}$ as a function of the duty cycle and frequency. The input signal amplitude is V_a = 0.3 V, the electrolyte is 1 mM HCl aqueous solution, the active area of the membrane is A = 0.32 cm^2. As in Figure 2d, here also $\Delta\bar{V}_{out}$ is practically zero for extreme duty cycles and low frequencies when the device is effectively at its steady state for significant parts of the temporal period. $\Delta\bar{V}_{out}$ increases with the input signal frequency reaching about -17 mV at a frequency of 250 Hz and a duty cycle of 0.6. Although the RBIP output increases with frequency within this range, it decreases for higher frequencies (Supplementary Figures 15 and 20).

$\Delta\bar{V}_{out}$ values for an aqueous 1 mM electrolyte were observed to be larger (in magnitude) than $\Delta\bar{V}_{out}$ values for an aqueous 10 mM electrolyte (Supplementary Note 7). Since the resistance for charge transport through the pore, R_p, effectively shunts $\bar{V}_{out}$ (Figure 1a), solutions with high ionic strength and membranes with a large pore diameter will tend to produce a lower RBIP output. The ionic strength of the solution also affects the double layer capacitances and the charging and discharging time constants at the RBIP surfaces leading to higher optimal frequencies (Supplementary Note 7). We observed that the diminished performance with higher concentration solutions can be partially mitigated using AAO membranes with smaller pores, but at the expense of higher overall ionic resistance per pore (Supplementary Note 7). Unlike previous demonstration of flashing ratchets, a non-negligible output was obtained for input signal amplitudes below 0.1 V (Supplementary Note 7). A discussion comparing the RBIP and prior flashing ratchet demonstrations can be found in Supplementary Note 10. Ratcheting was also demonstrated with $\Delta\bar{V}_{out}$ measured between two leak-free reference electrodes. Since reference electrodes measure the electric potential, this allows decoupling between the electric and chemical potentials that are induced by the ratchet (Supplementary Figure 17). More details on the measurement of $\Delta\bar{V}_{out}$ and the output dependence on different input signals and solution parameters can be found in Supplementary Note 2.

The buildup of $\bar{V}_{out}$ can result in the separation of cations and anions until columbic forces negate the ratchet action preventing further charge transport, or drive ambipolar transport.[21] To harness the ratchet induced voltage to drive a sustained net ionic current, charge neutrality must be maintained. This can be achieved by electrically shorting the two Ag/AgCl wires, which provides a low resistance path for removing chlorides from one compartment and generating them in the other. In this case, the current between the Ag/AgCl wires, I_{out}, is a result of oxidation of one silver wire and an aqueous chloride to form silver chloride, and reduction of silver chloride on the other wire to form silver and an aqueous chloride. The generation of chlorides in one compartment and their removal in the other balances deviations from electroneutrality due to ion pumping driven by charging and discharging of the RBIP contacts. Figure 3b shows the net ratchet induced current density output $\Delta\bar{I}_{out}/A$ as a function of the input signal duty cycle and frequency. As the voltage output, the current output shows a flashing rachet-like behavior with zero net output current at duty cycles of 0 and 1. Once an alternating input signal is injected to the device, a significant output current flows reaching as much as 3.15 μA/cm^2 at a frequency of 250 Hz and a duty cycle of 0.6. Supplementary Figure 7 and Figures S8c-d show the average temporal response and the extracted time constants for all frequencies and duty cycles.

To demonstrate the RBIP ability to drive ions against a force, a current-voltage scan was taken between the two Ag/AgCl wires while the ratchet is OFF ($V_{in} = 0$ V) and when it was ON with a duty cycle of 0.5 and a frequency of 100 Hz (Figure 3c). When the ratchet is OFF, the curve shows an expected linear ohmic behavior. However, when the ratchet is ON, the curve shifts by approximately the same $\Delta\bar{V}_{out}$ that was measured under the same conditions (Figure 3a), thus entering a quadrant in which ions are driven against an electrostatic force. It is interesting to analyze this result through the redox potentials of the Ag/AgCl wires. When the ratchet is OFF, the CV curve of the two Ag/AgCl wires follows a simple resistive form in which Cl^- is oxidized at the positively biased Ag/AgCl wire yielding an anodic current. However, once the ratchet is ON, the onset for this anodic reaction is shifted and Cl^- is oxidized even at voltages below 0 V. Complementary, the onset of the cathodic reaction is also shifted such that a negative overpotential of about 15 mV is required to drive a cathodic current. Since the current voltage curve is linear, the energetic efficiency of the RBIP is approximately $\eta = 0.25V_{oc}I_{sc}/\bar{P}_{in}$ where V_{oc} and I_{sc} are the open circuit voltage and the short circuit current as shown in Figure 3a,b respectively and $\bar{P}_{in}$ is the time averaged input power. At a frequency of 250 Hz and a duty cycle of 0.5, the input power is approximately 0.215 mW, and with the corresponding output from Figure 3a,b results in an efficiency of about $\eta = 1.96\cdot10^{-5}$.

Unlike conical nano-pores membranes that were shown to have a rectifying transport behavior,[6,7] our device demonstrates a linear current-voltage curve (Figure 3c and Supplementary Figure 30). This linearity confirms that current rectification is not required for RBIP operation. A detailed analysis of mechanisms that can potentially result in ionic current rectification is discussed in Supplementary Note 11, clarifying why in our devices neither the surface geometry nor the pore shape contributes to such behavior. Nevertheless, it is hypothesized that incorporating ionic current rectification, in addition to the capacitive ratchet mechanism, can result in enhanced performance. For example, by increasing the fill factor of the voltammograms in Figure 3c leading to more efficient devices (similar to photovoltaic cells).

The non-linear capacitance effects and the resulting ratcheting behavior were reproduced in simulation. The coupled Poisson-Nernst-Planck equations were solved for a one-dimensional system consisting of two electrolyte reservoirs separated by a membrane with a fixed pore charge. The two electrodes were modeled by defining the electric potential at the edges of the membrane. Supplementary Figure 12a shows a schematic illustration of the simulation domain, and Supplementary Figure 12b shows the spatial

distribution of the electric potential and ion concentration in the system during a typical time-period. The input signal alternated between 0.8 V and 0V and its frequency was 5 kHz. The solution was 0.5 mM KCl aqueous solution. Figure 3d shows the simulated output voltage considering three different membrane pore charges. As demonstrated experimentally, the time constants for charging and discharging the surfaces vary significantly with the input signal duty cycle and potential (Supplementary Figures 13-14). As a result, the net output voltage shows a ratcheting behavior: it approaches zero when a constant bias is applied (duty cycle of 0 or 1), but a significant time averaged voltage is obtained when an alternating input signal is introduced. The introduction of pore charge increases the output voltage and shifts the optimal duty cycle towards 1. Full details of the numerical model and the time constant extraction are given in the methods section and in Supplementary Note 6. Since the model is one-dimensional (i.e., it does not incorporate rectifying effects that arise in conical nano-pores), and since the simulation describes general physics of charging and discharging of the membrane surface, it can be concluded that the capacitive ratchet effect does not require a specific material or pore shape, and can be translated to material systems beyond those studied in this work.

Engineering devices for increased spatial asymmetry should result in increased asymmetric charging (and discharging) and thus enhanced performance. This can be achieved by varying the deposition process of the two metallic layers or using different materials. Asymmetric devices were fabricated by depositing gold on one surface of the AAO wafer and platinum on the other (a configuration that is termed Au-Pt). Figure 3e shows the extracted time constants for charging and discharging of the gold and platinum surfaces as a function of duty cycle. Although the input signal is the same as in Figure 1h, there is a larger difference between the charging (and discharging) time constants of the two electrodes. As a result, a dramatic increase in the output voltage (Figure 3f) and output current (Figure 3g) is observed. The measured signals and fitted curves are discussed in Supplementary Note 5. The input voltage is not equally distributed between the two contacts, and the electric potential of the platinum surface alternates with an amplitude that is almost double that of the gold surface (Supplementary Figure 9a,b). As discussed in the theoretical analysis (see Supplementary Note 14), if decoupled from the time constants for charging and discharging the surfaces, such an asymmetry can enhance device performance, yet it is not a prerequisite for device operation. Nevertheless, since the double layer capacitance is potential dependent, the higher effective amplitude of the potential applied to the Pt surface may contribute to the difference between the time constants between of the two surfaces leading to a higher device output. Other possible sources for asymmetry between the metal surfaces are differences in the surface chemistry, work functions (leading to differences in the point of zero charge), conductivity, and surface area. These sources for asymmetry may lead to differences in the charging-discharging time constants and differences in the amplitude of the potential that is effectively applied to the surfaces.

Ratchet Driven Electrodialysis

To demonstrate the RBIPs ion pumping functionality, we have demonstrated water deionization in a three-compartment electrodialysis system.[27] In this system, an RBIP is placed between two electrolyte reservoirs, with each reservoir connected to a central dilution cell by ion-selective membranes - a cation-exchange membrane (CEM) on one side and an anion-exchange membrane (AEM) on the other, thus forming a closed ionic circuit. Figure 4a shows a schematic illustration of the system. A photograph and a drawing of the setup are shown in Supplementary Figure 21a-b. When an input signal is applied to the RBIP, it induces a non-zero time-averaged voltage across it, driving transport of predominantly cations through the CEM and predominantly anions through the AEM. Electroneutrality is maintained by the

exchange of cations and anions through the RBIP itself. As a result, the initial 1 mM KCl concentration in all compartments decreases in the dilution cell, as indicated by a decrease in solution conductivity.

The conductance in the dilution cell was measured with two titanium wires, as described in the methods section and Supplementary Note 8, and the RBIP output voltage was monitored by measuring V_{out} between two Ag/AgCl wires (Figure 4a). The system was placed inside an incubator, to reduce temperature related conductance changes, and temperature was also measured at the side wall of the dilution cell (externally). To further account for temperature effects, the conductance was also measured in a reference cell, which has the same volume and geometry as the dilution cell and was located next to it. The electrolyte in all compartments was 1mM KCl aqueous solution, and the ratchet was driven with a rectangular wave of $V_a = 1\ \mathrm{V}$, $f = 11\ \mathrm{Hz}$, $d_c = 0.5$, which maximizes its output (Supplementary Figure 21c). Figure 4b shows the measured conductance in the dilution and reference cells normalized by their initial conductance. The absolute conductance and the measured temperature are shown in Supplementary Figure 24. When the input signal is switched 'On', V_{out} becomes negative, leading to a decrease in the solution conductivity (and the ion concentration) in the dilution cell. When the RBIP is switched 'Off', V_{out} drops in magnitude, and the conductivity in the dilution cell begins to increase, indicating transport of cations and anions back into the dilution cell concomitant with transport of ions across the RBIP for charge neutrality. These 'On'/'Off' cycles were repeated, demonstrating a clear causal relationship between RBIP operation and conductivity changes in the dilution cell. At its lowest point, the conductivity in the dilution cell was reduced by 50% ($t = 37\ \mathrm{h}$), while the conductivity in the reference cell remained nearly constant. Notably, the concentration gradient between the dilution cell and the reservoirs resulted in a buildup of V_{out} when the system was at rest (shaded areas in Figure 4b). A similar effect was used to probe the concentration difference in a second deionization experiment (see Supplementary Note 9). The RBIP output started to diminish after approximately 30 hours, resulting in a lower deionization rate. After 44 hours a rapid decline in performance was observed. The system was then allowed to rest until $t = 94\ \mathrm{h}$ in which back diffusion almost brought the conductivity to its equilibrium value. The consistent decrease in the conductance in the dilution cell when an input signal was applied thus validates the RBIPs ion pumping functionality.

Analytical Model

A simple analytical model predicts ratchet behavior similar to our experimental observations. The ratchet performance can be computed by assuming that the voltages V_L and V_R follow a charging and discharging behavior as in equation (3), and inserting them and the input signal into equation (1). The non-linear nature of the double layer impedance is approximated by assigning different time constants for the surfaces charging and discharging. Since these time constants are determined mostly by the duration of the charging and discharging period (Figure 2c, Supplementary Figure 5a), it can be assumed that $\tau_{L,2} = \tau_{R,2}$ and $\tau_{L,1} = \tau_{R,1}$. $\Delta\bar{V}_{out}$ was calculated using this procedure for various input signals and time constants. More details on the analytical model can be found in Supplementary Note 14. Figure 5a shows the normalized output, $\Delta\bar{V}_{out}/V_a$, as a function of the duty cycle for several input signal frequencies. The charging and discharging time constants are $\tau_{L,2} = \tau_{R,2} = 8\ \mathrm{ms}$, $\tau_{L,1} = \tau_{R,1} = 2\ \mathrm{ms}$ which are close to those extracted from experiment (Figure 2c). The output curves show a ratchet behavior with outputs near zero for extreme duty cycles and low frequencies, in which the temporal periods are significantly longer than the charging and discharging time constants. Like the experimental results, the output reaches

largest magnitudes at moderate duty cycles and higher frequencies. Figure 5b shows similar curves for $\tau_{L,2} = \tau_{R,2} = 100$ ms and $\tau_{L,1} = \tau_{R,1} = 1$ ms. For such an extreme difference in time constants, the output is higher and the optimal duty cycle shifts toward 0. In both cases, the output saturates when increasing the frequency. Figure 5c shows the maximal normalized output (in terms of absolute values) as a function of $\tau_{R,1}$ and $\tau_{R,2}$, with $\tau_{L,1} = \tau_{R,1}$ and $\tau_{L,2} = \tau_{R,2}$, and Figure 5d shows corresponding duty cycles. The parameters used in Figure 5a,b are marked with a triangle and a diamond respectively. When the RBIP capacitance is linear, i.e. all the time constants are equal, the output is zero. However, the output increases with the difference in time constants reaching magnitudes that approach $2V_a$ at optimal duty cycles that shift toward 0 or 1. Hence, for the highest performance, the time constants for charging and discharging must be as far apart as possible. It should be noted that devices with a geometrical asymmetry but with a linear capacitance, i.e. $\tau_{R,1} = \tau_{R,2}$ and $\tau_{L,1} = \tau_{L,2}$, produce a zero output. Thus, optimizing electrodes for high frequency dispersion is essential for efficient RBIP operation. In devices where $\tau_{L,1} \neq \tau_{R,1}$ and $\tau_{L,2} \neq \tau_{R,2}$, the maximal obtainable output is determined by the surface with the larger difference in time constants, and the effective amplitude acting on each surface (the amplitude asymmetry coefficient, a, as discussed in Supplementary Note 14). The larger the amplitude acting on one of the surfaces, the more dominant are the time constants of that surface in determining the total output (Supplementary Figure 39). In the Au-Pt device (Figure 3e-g), the time constants of the Pt surface are further apart (Figure 3e) and the amplitude of the voltage that the Pt surface fluctuates is larger (Supplementary Figure 9f) thus leading to a higher device performance.

The analytical model demonstrates that a non-linear capacitance, as observed in electric double layers, can result in a ratchet-like behavior. However, since the time constants in real devices vary significantly with the input signal properties, this model cannot predict the experimental performance of real devices and can only define optimal time constants for specific input signals. A detailed discussion of the model limitations can be found in Supplementary Note 14.

Scaling up RBIPs requires stable materials that can be processed on a large scale. Since the RBIP driving mechanism is not governed by the chemistry of specific materials, it can be expected that other membrane and electrode materials will also exhibit an RBIP functionality. Engineering surfaces for highly nonlinear capacitance while maintaining spatial asymmetry might be achievable without nano-scale precision thus allowing RBIP large area fabrication. Building on top of the suggested structures, more complex devices can be fabricated which support enhanced functionality. For example, layered structures can result in an ion pump driven with a flashing ratchet mechanism.[28] The energetic efficiency of flashing ratchet-based dialysis was compared to reverse osmosis and was shown to be higher under a wide range of conditions.[29] In addition, we showed that RBIPs can theoretically drive ions of the same charge, but different diffusion coefficients, in opposite directions as well as to transport both cations and anions in the same direction.[20,21] Such devices can pave the way towards ion selective pumps and single membrane dialysis systems. Further increasing the number of metal layers connected to independent voltage sources may allow tailoring the potential distribution within the pores which can further increase the device functionality and efficiency.[6]

In conclusion, we have realized a first-of-its-kind ion pump driven by a capacitive ratchet mechanism. This type of ion pump can drive a net ion flux in steady state with no redox reactions at the RBIP contacts. Ion pumping against an opposing force was demonstrated as well as electrolyte deionization. The driving mechanism stems from the non-linear capacitance of electrode double layers, which leads to deviation in time constants between charging and discharging. The demonstrated ion pump can pave the way for the

development of high efficiency desalination and selective ion separation systems, requiring neither moving parts nor redox reactions.

Acknowledgments

RK acknowledges the U.S. National Science Foundation Graduate Research Fellowship Program (DGE-1321846). AH acknowledges the support of the Boris Mints Institute. EJH acknowledges a Graduate Assistance in Areas of National Need (GAANN) Fellowship. CM acknowledges the gracious support for summer research at UC Irvine from Research Corporation for Science Advancement through a Cottrell Scholars Collaborative (Award #27512) awarded to SA and the UCI Vice Provost for Teaching and Learning. JWA was supported by the Joint Center for Artificial Photosynthesis, a DOE Energy Innovation Hub, supported through the Office of Science of the U.S. Department of Energy under Award No. DE-SC0004993. SA acknowledges the support of the Gordon and Betty Moore Foundation under a Moore Inventor Fellowship (GBMF grant #5641) and The Beall Family Foundation (UCI Beall Innovation Award). SA also acknowledges the Phase I Centers for Chemical Innovation (CCI) Program in the U.S. National Science Foundation Division of Chemistry under Grant CHE-2221599 for supporting collaborative student exchanges with the Sa Group at the University of Massachusetts Boston, as well as revisions to the initial manuscript submission.GS thanks the Azrieli Foundation for financial support within the Azrieli Fellows program. This work is partially funded by the European Union (ERC, ESIP-RM, 101039804). Views and opinions expressed are however those of the author(s) only and do not necessarily reflect those of the European Union or the European Research Council Executive Agency. Neither the European Union nor the granting authority can be held responsible for them. We would also like to acknowledge Prof. Reg Penner for allowing us to work with his group members and use their thermal evaporator for the fabrication of some of the RBIPs. We acknowledge the contribution of TAU Nano center for providing the sputtering and e-beam evaporation equipment, and the HRSEM. We thank G. Radovsky for taking the HRSEM images. We thank O. Nir and A. Chandra for guidance with the Electrodialysis setup.

Author contributions

GS, JWA and SA conceptualized this work, RK, AH, EJH, KSA, EG, RS, CM, DL and GS conducted the investigation, AH, SA and GS designed the methodology, RK, AH, EJH, KSA, RS, CM and GS conducted the formal analysis and acquired the data, visualizations were designed by EJH, AH, RK, SA and GS, the original draft was written by SA and GS, and all authors contributed to its reviewing and editing. GS and SA supervised the project, GS, SA and FMT administered it, and acquired the funding for it.

Competing Interests Statement

GS, JWA, FMT, and SA filed patent applications US 16/907,076 and US 17/125,341 for ratchet-based ion pumping membrane systems. There are no other conflicts of interest to declare.

Figures

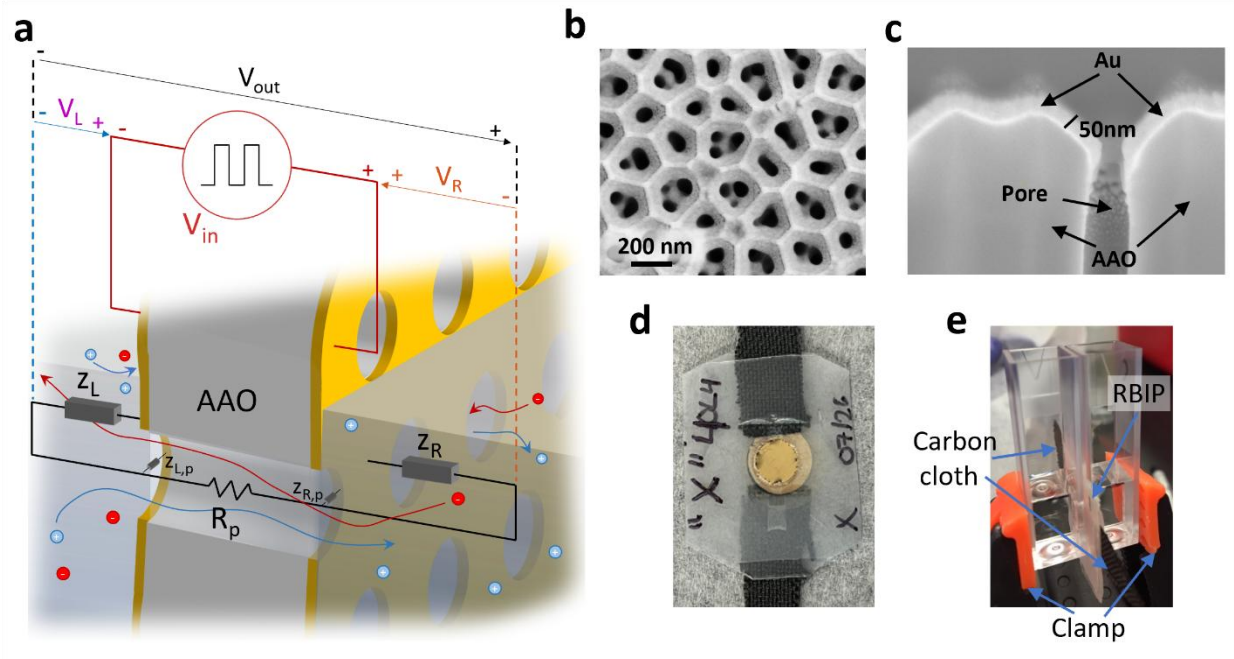

Figure 1: The RBIP*|(a) A schematic illustration of the RBIP structure and double layers impedances. (b-c) Plan and cross section view SEM images of fabricated RBIPs. respectively. (d) A photograph of a sample before its assembly. (e) A photograph of the RBIP performance characterization setup.*

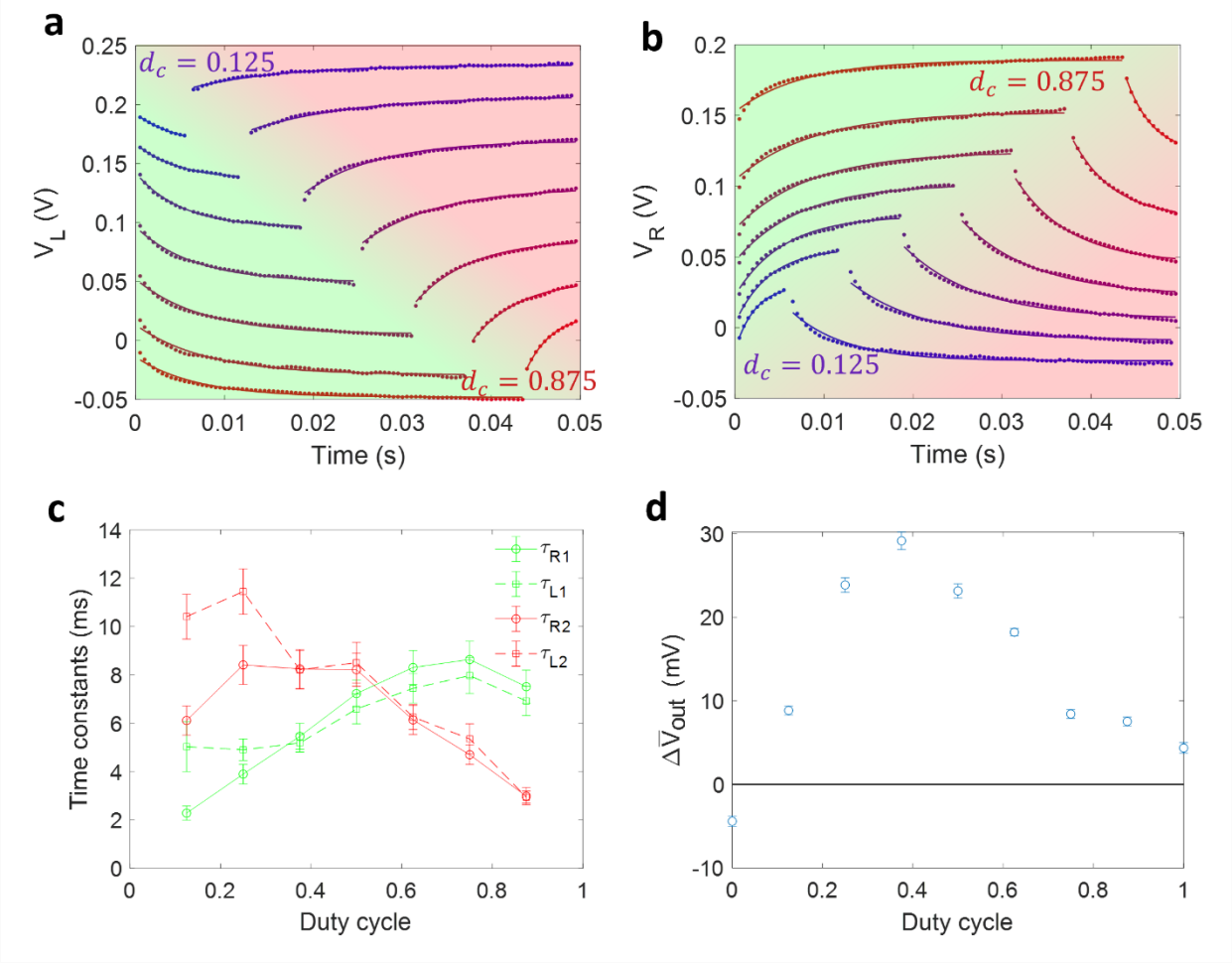

Figure 2: Non-linear capacitance| *(a-b) Experimentally measured signals $V_L(t)$ and $V_R(t)$, respectively, for rectangular-wave inputs with various duty cycles, d_c, over one time period, $T = 50\ ms$. The green areas are for the first portion of the period $0 < t \leq d_cT$ and the red areas are for the second portion of the period $d_cT < t \leq T$. The dots are the measurements, and the solid lines mark the best exponential fit to the data. The color coding marks the duty cycle. The electrolyte is 1 mM KCl aqueous solution, and the input signal is alternating between 300 mV and -300 mV. (c) Time constants extracted from the fitted curves in (a) and (b). Subscripts 1 and 2 denote that the time constants were extracted for the first ($0 < t \leq d_cT$) and second ($d_cT < t \leq T$) parts of the input signal, respectively. The error bars indicate the fitting 95% confidence interval. The number of samples used to fit the data was determined by input signal duty cycle and the measurement sampling rate with a minimum of 12 and a maximum of 87 data points. (d) The time averaged output voltage $\Delta\bar{V}_{out}$ as a function of the input signal duty cycle. $\Delta\bar{V}_{out}$ was obtained by averaging the per-period mean voltage of at least 480 temporal periods. The error bars are the standard deviation of the per-period mean voltages.*

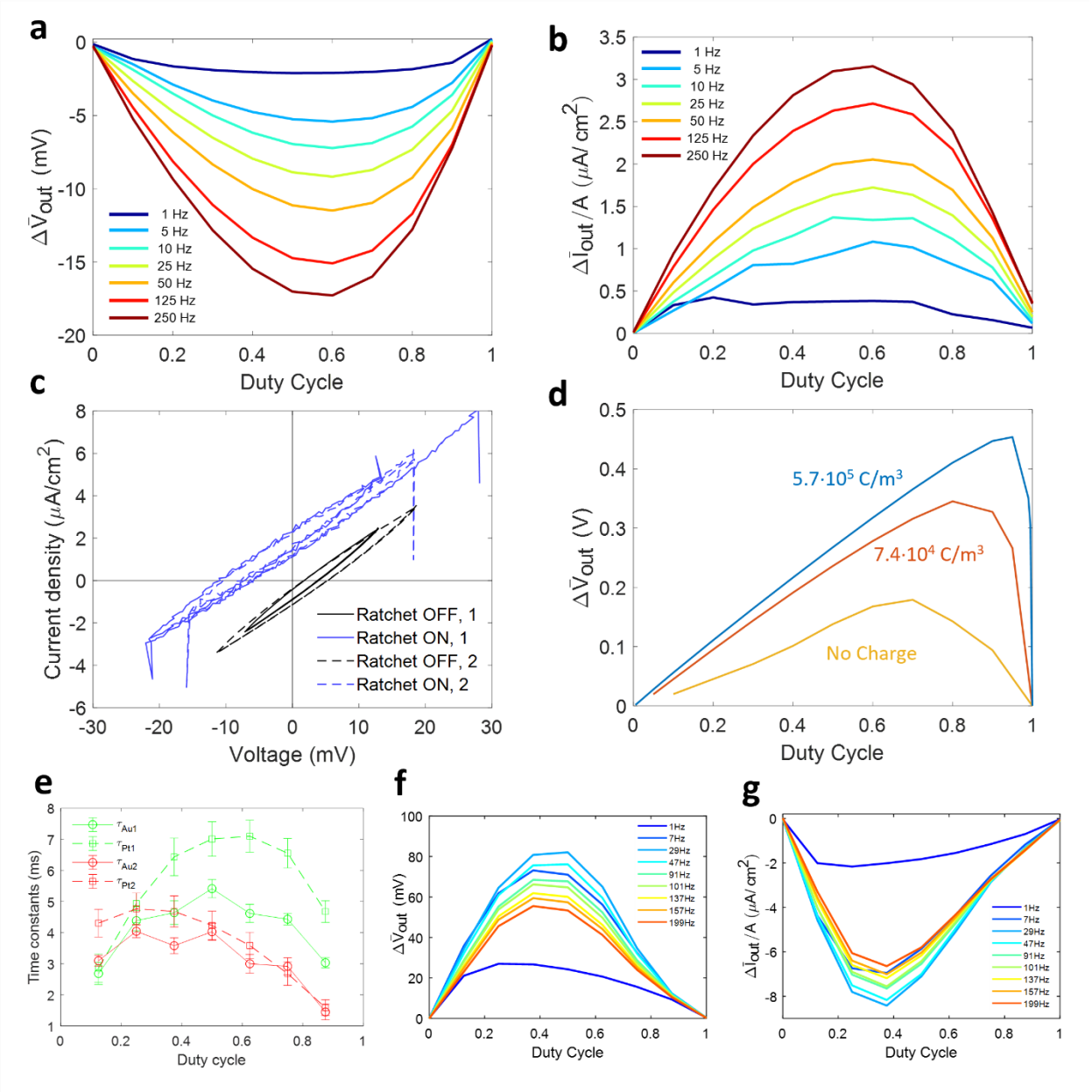

Figure 3: RBIP performance examination *| Au-Au RBIP net output voltage (a), and net output current density (b) as a function of the input signal duty cycle and frequency. (c) Current–Voltage curves ($\bar{I}_{out}/A$, $\bar{V}_{out}$) with Vin = 0 and with a square-wave input at a duty cycle of 0.5 and a frequency of 100 Hz. The input signal amplitude is V_a = 0.3 V and the electrolyte is 1 mM HCl aqueous solution. (d) Numerical simulation: net output voltage as a function of the input signal duty cycle for different membrane pore charges. V_{in} alternates between $0.8\ V$ to 0 V at a frequency of 5 kHz. (e) Au-Pt ratchet time constants as a function of the input signal duty cycle. The time constants were extracted from the signals shown in supplementary figure 9a-b. The number of samples used to fit the data was determined by input signal duty cycle and the measurement sampling rate with a minimum of 9 data points and a maximum of 85 data points. The error bars indicate the fitting 95% confidence interval. Au-Pt ratchet net output voltage (f), and net output current density (g), as a function of the input signal duty cycle and several frequencies. The input signal amplitude is V_a = 0.3 V and the electrolyte is 1 mM KCl aqueous solution.*

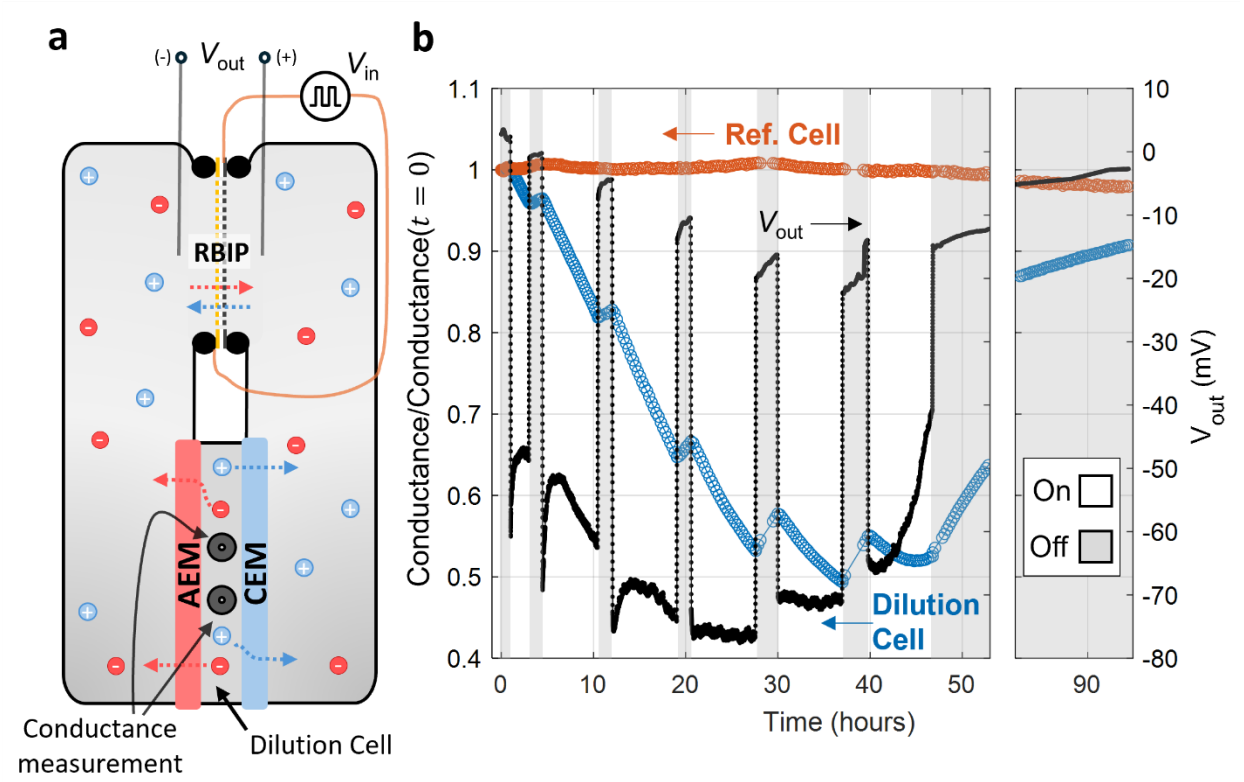

Figure 4: Electrodialysis (ED) deionization demonstration *|(a) Schematic illustration of the ED deionization system. V_{out} is measured between two Ag/AgCl wires with the indicated polarity, and conductance is measured in the dilution cell using two titanium wires, as detailed in the methods section. (b) Normalized conductance (relative to conductance at $t = 0$) in the dilution cell and reference cell (left y-axis), and output voltage across the RBIP (right y-axis), as a function of time. Bright areas are time periods in which the RBIP is continuously operating, and in the shaded areas the input voltage is set to 0 V. The input signal during RBIP operation is a square wave with: $V_a = 1\ V$, $f = 11\ Hz$, $d_c = 0.5$, and the electrolyte was initially 1 mM KCl aqueous solution in all compartments. Ratchet induced ion pumping resulted in a 50% reduction in the conductivity of the solution in the dilution cell. The volume of the dilution and reference cells is $0.63\ cm^3$ and $0.66\ cm^3$, respectively.*

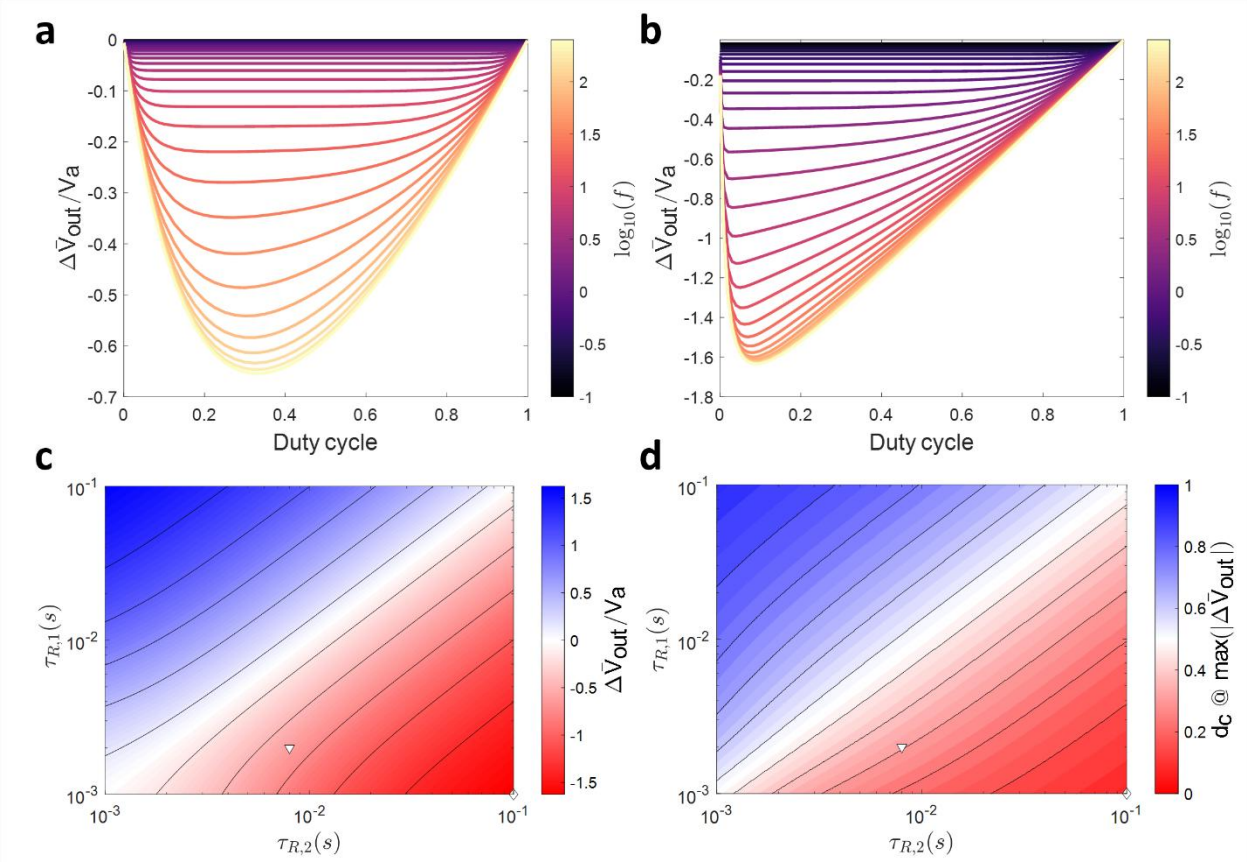

Figure 5: *Analytical model | (a) The ratchet normalized output, $\Delta\bar{V}_{out}/V_a$, as a function of the input signal duty cycle for several input signal frequencies, $\tau_{L,2} = \tau_{R,2} = 8$ ms, $\tau_{L,1} = \tau_{R,1} = 2$ ms, and $V_a = 0.3\ V$. (b) $\Delta\bar{V}_{out}/V_a$ as a function of the input signal duty cycle for several input signal frequencies, $\tau_{L,2} = \tau_{R,2} = 100$ ms, $\tau_{L,1} = \tau_{R,1} = 1$ ms, and $V_a = 0.3\ V$. (c) The RBIP normalized output, $\Delta\bar{V}_{out}/V_a$, as a function of $\tau_{R,1}$ and $\tau_{R,2}$. For each combination of time constants the duty cycle is optimized to obtain the highest output. The input signal frequency is 100 Hz. (d) The duty cycles for which the magnitude of $\bar{V}_{out}$ is maximal. The triangle and the diamond mark the parameters used in a and b respectively.*

References

1. Kedem, O., Lau, B. & Weiss, E. A. How to Drive a Flashing Electron Ratchet to Maximize Current. *Nano Lett.* **17**, 5848–5854 (2017).
2. Reimann, P. Brownian motors: Noisy transport far from equilibrium. *Phys. Rep.* **361**, 57–265 (2002).
3. Dean Astumian, R. Stochastically pumped adaptation and directional motion of molecular machines. *Proc. Natl. Acad. Sci. U. S. A.* **115**, 9405–9413 (2018).
4. Roeling, E. M. *et al.* Organic electronic ratchets doing work. *Nat. Mater.* **10**, 51–55 (2011).
5. Tarlie, M. B. & Astumian, R. D. Optimal modulation of a Brownian ratchet and enhanced sensitivity to a weak external force. *Proc. Natl. Acad. Sci.* **95**, 2039–2043 (2002).
6. Parrondo, J. M. R., Blanco, J. M., Cao, F. J. & Brito, R. Efficiency of Brownian motors. *Europhys. Lett.* **43**, 248–254 (1998).
7. Kedem, O., Lau, B. & Weiss, E. A. Mechanisms of Symmetry Breaking in a Multidimensional Flashing Particle Ratchet. *ACS Nano* **11**, 7148–7155 (2017).
8. Kedem, O., Lau, B., Ratner, M. A. & Weiss, E. A. Light-responsive organic flashing electron ratchet. *Proc. Natl. Acad. Sci.* **114**, 8698–8703 (2017).
9. Squires, T. M. Induced-charge electrokinetics : fundamental challenges and opportunities. *Lab Chip* 2477–2483 (2009) doi:10.1039/b906909g.
10. Schwemmer, C., Fringes, S., Duerig, U., Ryu, Y. K. & Knoll, A. W. Experimental Observation of Current Reversal in a Rocking Brownian Motor. *Phys. Rev. Lett.* **121**, 104102 (2018).
11. Nicollier, P. *et al.* Nanometer-Scale-Resolution Multichannel Separation of Spherical Particles in a Rocking Ratchet with Increasing Barrier Heights. *Phys. Rev. Appl.* **15**, 034006 (2021).
12. Skaug, M. J., Schwemmer, C., Fringes, S., Rawlings, C. D. & Knoll, A. W. Nanofluidic rocking Brownian motors. *Science (80-.).* **359**, 1505–1508 (2018).
13. Słapik, A., Łuczka, J., Hänggi, P. & Spiechowicz, J. Tunable Mass Separation via Negative Mobility. *Physical Review Letters* vol. 122 at https://doi.org/10.1103/PhysRevLett.122.070602 (2019).
14. Motz, T., Schmid, G., Hänggi, P., Reguera, D. & Rubí, J. M. Optimizing the performance of the entropic splitter for particle separation. *J. Chem. Phys.* **141**, 074104 (2014).
15. Reguera, D. *et al.* Entropic splitter for particle separation. *Phys. Rev. Lett.* **108**, 1–5 (2012).
16. Yang, B., Long, F. & Mei, D. C. Negative mobility and multiple current reversals induced by colored thermal fluctuation in an asymmetric periodic potential. *Eur. Phys. J. B* **85**, 2–7 (2012).
17. Siwy, Z. & Fuliński, A. A nanodevice for rectification and pumping ions. *Am. J. Phys.* **72**, 567–574 (2004).
18. Siwy, Z. & Fuliński, A. Fabrication of a Synthetic Nanopore Ion Pump. *Phys. Rev. Lett.* **89**, 4–7 (2002).
19. Wu, X., Ramiah Rajasekaran, P. & Martin, C. R. An Alternating Current Electroosmotic Pump

Based on Conical Nanopore Membranes. *ACS Nano* **10**, 4637–4643 (2016).

20. Herman, A. A. *et al.* Ratchet-Based Ion Pumps for Selective Ion Separations. *PRX Energy* **2**, 023001 (2023).

21. Herman, A. & Segev, G. Ambipolar Ion Pumping with Ratchet Driven Active Membranes. *Phys. Rev. Appl.* **21**, 034056 (2024).

22. Bazant, M. Z., Thornton, K. & Ajdari, A. Diffuse-charge dynamics in electrochemical systems. *Phys. Rev. E* **70**, 24 (2004).

23. Kerner, Z. & Pajkossy, T. On the origin of capacitance dispersion of rough electrodes. *Electrochim. Acta* **46**, 207–211 (2000).

24. Pajkossy, T. Impedance spectroscopy at interfaces of metals and aqueous solutions — Surface roughness, CPE and related issues. *Solid State Ionics* **176**, 1997–2003 (2005).

25. Pajkossy, T. Impedance of rough capacitive electrodes. *J. Electroanal. Chem.* **364**, 111–125 (1994).

26. Lasia, A. Electrochemical Impedance Spectroscopy and its Applications. in *Modern Aspects of Electrochemistry* 143–248 (Kluwer Academic Publishers, Boston). doi:10.1007/0-306-46916-2_2.

27. White, W., Sanborn, C. D., Fabian, D. M. & Ardo, S. Conversion of Visible Light into Ionic Power Using Photoacid-Dye-Sensitized Bipolar Ion-Exchange Membranes. *Joule* **2**, 1–16 (2017).

28. Lau, B. & Kedem, O. Electron ratchets: State of the field and future challenges. *J. Chem. Phys.* **152**, 200901 (2020).

29. Marbach, S., Kavokine, N. & Bocquet, L. Resonant osmosis across active switchable membranes. *J. Chem. Phys.* **152**, (2020).

Data Availability

The source data for all the main text figures are provided with this paper. All other data are available from the corresponding authors upon request.

Methods

Sample preparation

RBIP samples were fabricated by depositing metal contacts on both surfaces of annealed anodized aluminum oxide (AAO) wafers (InRedox Materials Innovation) with thickness 50 µm, and pore diameters of 20 nm, 40 nm, or 60 nm. The wafers were air annealed for ~10 h at a temperature of 650 °C. Several RBIP structures and recipes were tested all showing the RBIP functionality. The samples discussed in Figure 3a-b were made of AAO wafers with a pore diameter of 40 nm and their contacts were deposited with thermal evaporation of a chrome adhesion layer and then gold. The thickness of both layers was 40 nm (planar equivalent). The samples discussed in Figure 3e-g and Figure 4 had a pore diameter of 40 nm and 60 nm respectively. The platinum contact was deposited with an electron beam evaporator and the gold contact was deposited with magnetron sputtering. The thickness of both contacts was 50 nm (planar equivalent). The sample discussed in Figure 1 had a pore diameter of 60 nm and the metal contacts were

deposited with magnetron sputtering of gold on both sides of the wafer (50 nm planar equivalent) followed by an 8 nm thick TiO_2 coating deposited by ALD. The ALD recipe is as described by Vega et al.[30] where the exposure time to the precursors was set to 1 s and the purging time was set to 5 s. The edges of the sample were masked during the ALD process to allow contacting the sample. The metal contacts in the samples described in Figures S15, S20 were deposited with electron beam evaporation of a 10 nm thick titanium adhesion layer and then 40 nm of gold. The RBIP ion pumping properties were tested in an electrochemical cell in which the RBIP served as a membrane separating two aqueous electrolyte compartments, each containing an Ag/AgCl wire that was used to probe the voltage or current between the two compartments. In the experiments shown in Figures 2a-b, and in Figures S6-8,S16,S25-28,S34 the electrochemical cell was as shown in Figure 1e, where parafilm was used to secure the wafers and prevent leakage (Supplementary Figure 1), and Carbon black cloth to contact the RBIP electrodes (no contact with the electrolyte). The RBIP active area was 0.32 cm^2. The electrodialysis cell discussed in Figure 4 was made of Formlabs Clear V4 resin. In all other experiments the electrochemical cell was constructed from PEEK, with Silicone rubber used to secure the wafers and prevent leakage, and ZOFLEX® CD45.1 conductive foam and copper tape to contact the RBIP electrodes (no contact with electrolyte). Here the RBIP active area was 0.16 cm^2.

RBIP performance characterization

To ensure that all the observed performance is a result of a ratcheting mechanism, as opposed to artifacts induced by unwanted electronic feedbacks, all measurement instruments and power sources were electrically floating (i.e., no part of the system was grounded), and all input signals and measurements were performed in two electrode setups. In Figures 2a-b the input signal was produced with a BioLogic VSP-300 multichannel potentiostat. The voltage and current measurements were conducted with a separate channel from the same potentiostat. Voltage measurements were taken with a sampling time of 200 µs and current measurements were taken with a sampling time of 400 µs. All the potentiostat channels were in floating mode. The RBIP performance discussed in Figure 3a-b was characterized using the following procedures. First, V_{in} was set to 0 V for 30 s. Next, the ratchet signal was introduced for 90 s. Finally, V_{in} was set to 0 V for another 60 s. The ratchet induced voltage $\Delta\bar{V}_{out}$ was calculated according to $\bar{V}_{out} = \bar{V}_{out,ON} - (\bar{V}_{out,OFF_1} + \bar{V}_{out,OFF_2})/2$ and the ratchet induced current $\Delta\bar{I}_{out}$ was calculated according to $\bar{I}_{out} = \bar{I}_{out,ON} - (\bar{I}_{out,OFF_1} + \bar{I}_{out,OFF_2})/2$. $\bar{V}_{out,ON}$ and $\bar{I}_{out,ON}$ are respectively the voltage and current averaged over the last 30 s of the period in which the input signal was applied. $\bar{V}_{out,OFF_1}$ and $\bar{I}_{out,OFF_1}$ are respectively the voltage and current averaged over the last 15 s in the first (30 s long) period in which V_{in} = 0 V. $\bar{V}_{out,OFF_2}$ and $\bar{I}_{out,OFF_2}$ are respectively the voltage and current averaged over the last 30 s of the second OFF period.

In Figure 2, Figure 3e-g, Figure 4b, and Supplementary Figure 21c the input signal was supplied with a Keysight 33510B waveform generator and voltages were measured with Keysight 34465A multimeters. In Figure 2 and Figures 3f-g the response to every input signal was measured for 60 s after which the input was set to 0 V for 60 s. In Figures 2a-b the voltage V_L was measured between the left gold contact and the adjacent Ag/AgCl wire, V_{out} was measured between the two Ag/AgCl wires, and V_R was calculated using equation (1). The mean temporal signals, $V_L(t)$ and $V_R(t)$, were found by obtaining the mean responses out of 300 periods. The sampling time was $5 \cdot 10^{-4}$ s. Supplementary Figure 3 shows an example of the measured signal and the $\Delta\bar{V}_{out}$ calculation shown in Figure 1i. In Figures 3f-g the

voltage and current measurements were conducted with a sampling time of $6 \cdot 10^{-4}$ s. The net output voltage and current were calculated according to the method described above for Figures 3a-b, where the averaged voltage and current were obtained by averaging measurements between 0.85 and 0.95 of each ON/OFF period. In Figure 4b the voltage measurement was conducted with an integration time of 2 s to reduce the output signal oscillations and obtain only the net averaged voltage. The sampling time was 4 s. In Supplementary Figure 21c data was recorded with an integration time of $1 \cdot 10^{-4}$ s and sampling time of $2 \cdot 10^{-4}$ s.

In some samples, input of a constant bias higher than ±300 mV resulted in a constant, non-negligible V_{out}. This may suggest Faradaic reactivity, which was followed by degradation in the RBIP performance for some samples (Supplementary Note 12). In other samples, non-zero V_{out} under a constant bias was attributed to blocked pores (Supplementary Note 13).

Numerical Simulation

The electric potential and ion concentrations in response to a rectangular wave input signal was computed by solving the one-dimensional Poisson-Nernst-Planck (PNP) equations using COMSOL Multiphysics® v6.1. The model geometry is illustrated in Supplementary Figure 12a. The simulation domain consists of two electrolyte reservoirs (thickness $W = 4.5\ \mu\mathrm{m}$) which are separated by the RBIP membrane (thickness $L = 1\ \mu\mathrm{m}$). The RBIP electrodes are modeled as point contacts (0D) and the boundary conditions at the edges of the simulation domain were of zero flux thus modeling closed reservoirs. Simulations were performed assuming a symmetric binary 1:1 electrolyte with equal diffusion coefficients ($D = 2 \cdot 10^{-9}\ \mathrm{m}^2/\mathrm{s}$) for both ion species, no faradaic reactions at the electrodes and no solvent convection. A full description of the governing equations, boundary conditions, input signal, meshing, simulation sequence and membrane surface charge calculation, is given in Supplementary Note 6.

Conductance measurements within the electrodialysis experiment

Real-time solution conductance measurements were carried out by embedding two titanium electrodes into the dilution cell in the electrodialysis setup. Similar to two-electrode conductivity meters, the conductance was obtained by applying a sine wave voltage signal between the two electrodes and measuring the resulting sinusoidal current flowing through the electrolyte. A detailed description of the test methodology and measurement setup is given in Supplementary Note 8.

Methods-only references

30. Vega, V. *et al.* Diffusive transport through surface functionalized nanoporous alumina membranes by atomic layer deposition of metal oxides. *J. Ind. Eng. Chem.* **52**, 66–72 (2017).